Journal of Materials Chemistry A

ROYAL SOCIETY OF CHEMISTRY

PAPER

View Article Online
View Journal

Cite this: DOI: 10.1039/d6ta00399k

Quinone redox centers enable charge localization and oxygen activation for high-efficiency H_2O_2 photosynthesis in covalent organic frameworks

Wan Zhang,†[a] Miao Sun,†[b] Lei Wang,*[a] Xiaojun Wu [b] and Hangxun Xu *[a]

Covalent organic frameworks (COFs) offer a crystalline and designable platform for photocatalytic hydrogen peroxide (H_2O_2) production, yet their efficiencies are often limited by inefficient utilization of photogenerated charges and the lack of chemically defined oxygen reduction centers. Here we show that quinone redox centers enable charge localization and oxygen activation for high-efficiency H_2O_2 photosynthesis by constructing a π-conjugated COF platform and directly comparing an anthraquinone-containing COF (AQ-HPTP COF) with an anthracene analogue (AN-HPTP COF) as a non-redox control within an identical hxl topology. Under visible light irradiation, AQ-HPTP COF exhibits an exceptional solar-to-chemical conversion efficiency of 2.10%, making it among the highest-performing COF photocatalysts reported for H_2O_2 photosynthesis. Spectroscopic characterizations combined with theoretical calculations reveal that quinone incorporation induces pronounced frontier-orbital separation and preferential localization of photoexcited electrons at the center, thereby facilitating charge separation and increasing charge utilization. In addition, proton-coupled reduction of the quinone enhances oxygen binding and promotes efficient and selective oxygen reduction toward H_2O_2. These results establish a general design principle in which integrating programmable quinone redox centers into COF lattices enables the concurrent optimization of charge dynamics and catalytic activity for solar-to-chemical energy conversion.

Received 15th January 2026
Accepted 14th March 2026

DOI: 10.1039/d6ta00399k

rsc.li/materials-a

1 Introduction

Hydrogen peroxide (H_2O_2) is a high-value oxidant and energy carrier with broad applications in environmental remediation, chemical synthesis, semiconductor manufacturing, and emerging energy technologies.[1,2] Yet over 95% of H_2O_2 currently is produced by the anthraquinone (AQ) process, an energy- and infrastructure-intensive route that relies on cyclic hydrogenation/oxidation and centralized production.[3,4] Solar-driven H_2O_2 synthesis from water and oxygen is an attractive alternative, but practical deployment is limited by modest solar-to-chemical conversion (SCC) efficiencies.[5–7] This challenge primarily originates from inefficient utilization of photogenerated charge carriers and the lack of precisely defined oxygen reduction reaction (ORR) active sites.

Covalent organic frameworks (COFs) are a prominent class of reticular materials for addressing these bottlenecks.[8,9] Their modular construction, high crystallinity, and tunable electronic structures enable the rational optimization of charge carrier dynamics and the programmable installation of catalytically active sites, features that are particularly advantageous for photocatalytic H_2O_2 production.[10–12] Despite rapid progress in recent years, however, most COF photocatalysts still suffer from inefficient photogenerated charge utilization, and achieving SCC efficiencies beyond 2% remains a persistent challenge.[13–15] Therefore, strategies that simultaneously enhance charge dynamics and precisely engineer selective ORR active sites are essential to unlock the full potential of COFs for solar-driven H_2O_2 photosynthesis.

Inspired by the industrial AQ process, quinone motifs have been widely integrated into polymer photocatalysts as programmable ORR centers to promote selective two-electron O_2 reduction toward H_2O_2.[16–18] Extending this concept to highly crystalline COFs, however, remains challenging as most reported AQ-containing COFs rely on keto–enamine linkages and predominantly adopt the hcb topology.[19–21] As a result, charge dynamics and catalytic function are not simultaneously optimized for solar-driven H_2O_2 photosynthesis. Since COF topology determines electronic coupling, exciton dissociation, and carrier transport, it set an intrinsic upper limit on how effectively photogenerated charges are utilized for photocatalysis.[22,23] In this context, the hxl topology features a higher

[a]Hefei National Research Center for Physical Sciences at the Microscale, Department of Polymer Science and Engineering, University of Science and Technology of China, Hefei, Anhui 230026, China. E-mail: lwang@ustc.edu.cn; hxu@ustc.edu.cn

[b]Key Laboratory of Precision and Intelligent Chemistry, Department of Materials Science and Engineering, University of Science and Technology of China, Hefei, Anhui 230026, China

† These authors contributed equally to this work.

density of π-conjugated segments and stronger in-plane electronic coupling, which collectively increase band dispersion and reduce the effective masses of charge carriers.[24] Consequently, exciton dissociation and charge transport can be improved simultaneously, leading to more efficient charge separation and migration and, ultimately, enhanced photocatalytic performance. This perspective implies that the photocatalytic performance of many existing AQ-incorporated COFs may be constrained by the topological framework that regulates charge transport to the catalytic AQ moiety. Consequently, integrating topological effects into COF design offers a viable route to maximize charge utilization and realize high-efficiency solar-driven H_2O_2 photosynthesis.

In this study, we report two π-conjugated sp^2 carbon-linked COFs with the hxl topology, namely AQ-HPTP COF integrating an anthraquinone redox center and AN-HPTP COF bearing an anthracene (AN) analogue as a non-redox control. In this manner, we are able to elucidate how a quinone active site regulate excited charge dynamics and ORR kinetics within an identical topological framework. Density functional theory (DFT) calculations reveal pronounced separation of the lowest unoccupied molecular orbital (LUMO) and the highest occupied molecular orbital (HOMO) and preferential localization of photoexcited electrons on the AQ moiety, an effect absents in AN-HPTP COF. Temperature-dependent photoluminescence (PL) and Hall effect measurements further indicate a reduced exciton binding energy (E_b) and enhanced carrier mobility for AQ-HPTP COF, collectively enabling markedly improved photogenerated charge utilization. As a result, AQ-HPTP COF achieves an exceptional SCC efficiency of 2.10%, substantially outperforming AN-HPTP COF and ranking among the most efficient COFs reported to date for solar-driven H_2O_2 photosynthesis. Moreover, it is found that proton-coupled reduction of the AQ moiety significantly lowers the O_2 adsorption energy, thereby accelerating oxygen activation and ensuring two-electron ORR toward H_2O_2. These findings demonstrate that integrating quinone redox centers into topology-optimized frameworks is an effective strategy to overcome charge utilization limits and advance COFs for solar-to-chemical energy conversion.

2 Results and discussion

AQ-HPTP COF and AN-HPTP COF were synthesized *via* Knoevenagel condensation between 2,3,6,7,10,11-hexakis(4-formylphenyl)triphenylene (HFPTP) and acetonitrile monomers containing AQ and AN moieties, respectively (Fig. 1a).[25] Fourier-transform infrared (FTIR) spectra provide clear evidence of complete condensation, as the aldehyde C–H stretching bands of HFPTP at 2830 and 2731 cm^{-1} and the aldehyde C═O stretching vibration at 1700 cm^{-1} disappear after polymerization (Fig. 1b).[26] Concomitantly, the C≡N stretching vibration of the acetonitrile precursors shifts from ~2249 to ~2214 cm^{-1}, consistent with formation of the cyanovinylene linkage (–C═C(CN)–) in both COFs.[27] In AQ-HPTP COF, the presence of carbonyl stretching band at 1670 cm^{-1} further confirms successful incorporation of the AQ moiety into the COF skeleton.[17]

X-ray photoelectron spectroscopy (XPS) further substantiates the chemical structures. In the C 1s region, both COFs show characteristic peaks for sp^2 (C═C) and sp (C≡N) hybridized carbons at 284.8 and 286.4 eV, respectively (Fig. 1c).[24] A distinct C═O component at 287.5 eV is observed exclusively for AQ-HPTP COF, confirming quinone incorporation.[28] Consistently, the O 1s spectrum of AQ-HPTP COF exhibits a characteristic peak at 531.6 eV which is attributed to the carbonyl oxygen (Fig. S1).[29] Solid-state ^{13}C cross-polarization magic-angle-spinning (CP-MAS) NMR spectroscopy provides complementary verification. As shown in Fig. 1d, resonance peaks at ~117 and ~110 ppm are assigned to the cyanovinylene linkage in both COFs while the additional peak at 182 ppm in AQ-HPTP COF is distinct feature for the carbonyl carbon.[30] These spectroscopic signatures confirm the successful construction of AQ-HPTP COF and AN-HPTP COF with identical cyanovinylene-linked backbones and well-defined differences in redox functionality.

The crystallinity and stacking mode of both COFs were examined by powder X-ray diffraction (PXRD). AQ-HPTP COF exhibits diffraction peaks at 2.70°, 4.62°, 5.45°, and 8.18°, which can be indexed to the (100), (110), (200), and (300) planes, respectively (Fig. 2a). AN-HPTP COF displays analogous peaks at 2.72°, 4.67°, 5.52°, and 8.22°, corresponding to the (100), (110), (200), and (300) planes, respectively (Fig. 2b). Moreover, both COFs exhibit similar crystalline domain sizes, as shown in Fig. S2 and Table S1. The experimental PXRD patterns match closely with simulations based on the AA stacking model (Fig. S3) and deviate substantially from the AB stacking model (Fig. S4), supporting an eclipsed stacking arrangement.[31] Pawley refinement yields unit cell parameters of $a = b = 40.04$ Å, $c = 3.44$ Å, $\alpha = \beta = 90°$, $\gamma = 120°$ ($R_{wp} = 3.23\%$, $R_p = 2.44\%$) for AQ-HPTP COF and $a = b = 39.99$ Å, $c = 3.44$ Å, $\alpha = \beta = 90°$, $\gamma = 120°$ ($R_{wp} = 4.38\%$, $R_p = 3.40\%$) for AN-HPTP COF, confirming that both COFs adopt highly ordered crystalline lattices with essentially identical long-range structures.

N_2 adsorption/desorption measurements were conducted to evaluate the porosity and pore structure of both COFs. As displayed in Fig. 2c and d, both AQ-HPTP COF and AN-HPTP COF show typical type-IV isotherms characteristic of mesoporous frameworks.[32] The Brunauer–Emmett–Teller (BET) surface areas are found to be 634.89 $m^2\ g^{-1}$ for AQ-HPTP COF and 609.30 $m^2\ g^{-1}$ for AN-HPTP COF. The pore size distributions for AQ-HPTP COF and AN-HPTP COF are both centered at around 2.5–2.9 nm, in good agreement with values predicted from the AA stacking model. Electron microscopy further revealed comparable morphologies. Scanning electron microscopy (SEM) and transmission electron microscopy (TEM) images show tubular assemblies constructed from stacked nanosheets (Fig. S5 and S6). High-resolution TEM resolves well-ordered channels in both COFs, with measured diameters of 2.80 nm for AQ-HPTP COF and 2.78 nm for AN-HPTP COF, consistent with the results from the N_2 adsorption/desorption measurements (Fig. 2e, f, and S7). Both frameworks exhibit excellent thermal stability, as expected for sp^2 carbon-linked frameworks

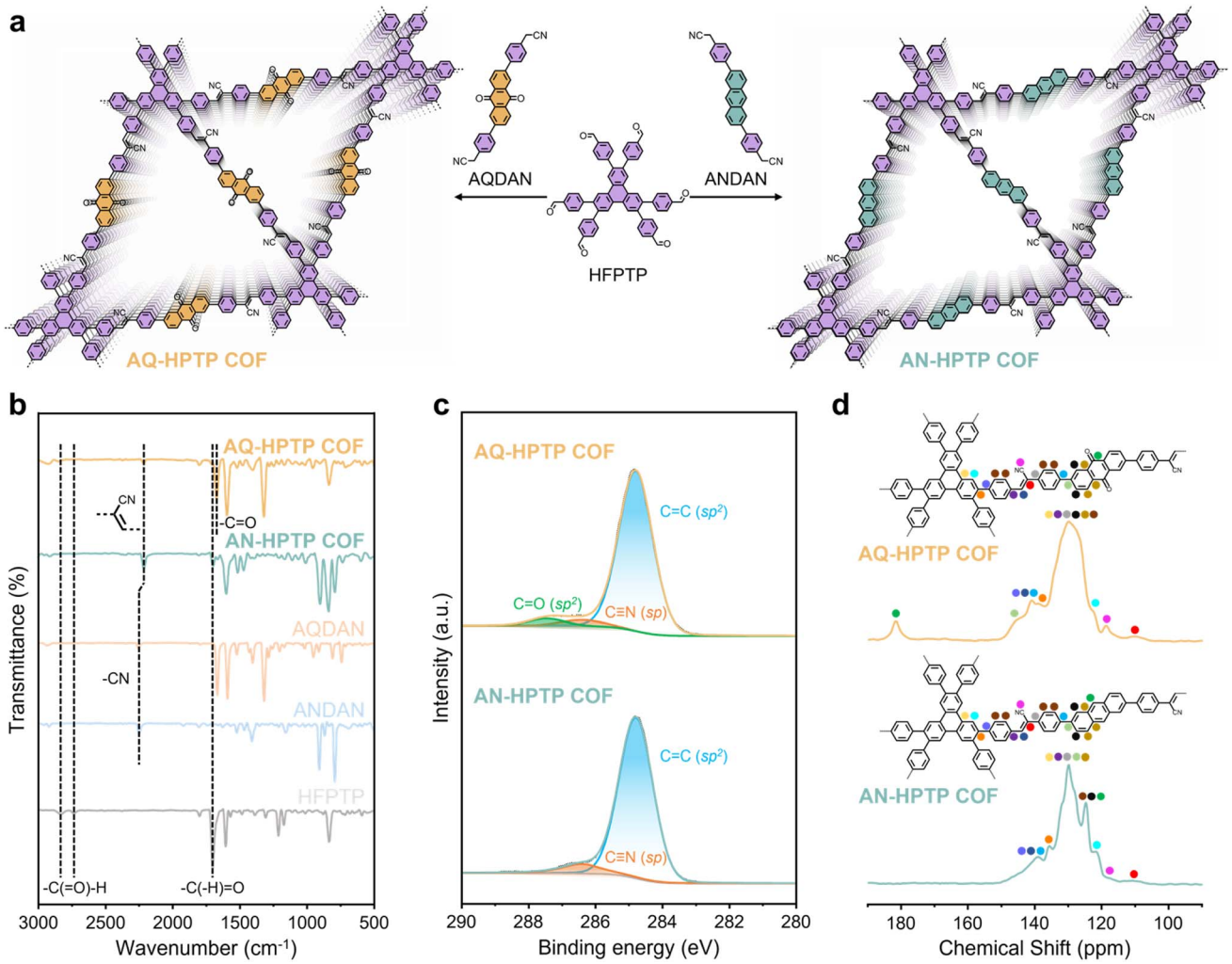

Fig. 1 (a) Synthetic routes and corresponding chemical structures of AQ-HPTP COF and AN-HPTP COF. (b) FTIR, (c) high-resolution C 1s XPS, and (d) solid-state ^{13}C CP-MAS NMR spectra of AQ-HPTP COF and AN-HPTP COF.

(Fig. S8). They also display nearly identical water contact angles, indicating comparable surface wettability (Fig. S9).

The electronic band structure of a photocatalyst dictates the thermodynamic driving force for interfacial redox reactions and therefore strongly influences photocatalytic performance. The electronic structures of AQ-HPTP COF and AN-HPTP COF were characterized by UV-vis diffuse reflectance spectra and synchrotron radiation photoelectron spectroscopy (SRPES). Both COFs exhibit strong visible-light absorption (Fig. 3a), with optical bandgaps of 2.64 eV for AQ-HPTP COF and 2.52 eV for AN-HPTP COF. SRPES reveals valence band (VB) positions of −6.31 eV for AQ-HPTP COF and −6.16 eV for AN-HPTP COF (Fig. S10). Combining these VB levels with the optical bandgaps leads to corresponding conduction band (CB) position and thus the complete band structures (Fig. 3b). Considering the redox potentials of $O_2/\cdot O_2^-$ (−3.69 eV), O_2/H_2O_2 (−4.70 eV), H_2O/O_2 (−5.25 eV) and H_2O/H_2O_2 (−5.78 eV), both COFs provide sufficient energetic driving forces for photocatalytic H_2O_2 production *via* direct two-electron ORR, coupled with two-electron or four-electron water oxidation reaction (WOR).[33]

Photocatalytic H_2O_2 production was then assessed in O_2-saturated pure water under visible light irradiation ($\lambda > 420$ nm, 300 W Xe lamp). As shown in Fig. 3c, AQ-HPTP COF delivers a prominent H_2O_2 production rate of 7008 μmol g^{-1} h^{-1}, which is 3.2-fold higher than that of AN-HPTP COF (2208 μmol g^{-1} h^{-1}) under identical conditions. The formation of H_2O_2 on both COF surfaces was monitored by *in situ* diffuse reflectance infrared Fourier transform spectroscopy (DRIFTS) (Fig. S11). A newly emerged IR peak at 2840 cm^{-1}, attributed to the characteristic O–H stretching vibration of H_2O_2, grows steadily with irradiation time, confirming *in situ* generation of H_2O_2. After normalization, AQ-HPTP COF shows a markedly faster increase of this feature than AN-HPTP COF (Fig. S12), consistent with the catalytic rates shown in Fig. 3c and highlighting the critical role of AQ moiety in promoting H_2O_2 photosynthesis. Both COFs retain essentially unchanged activity over five consecutive cycles, indicating excellent stability (Fig. 3c). Post-reaction FTIR, solid-state ^{13}C CP-MAS NMR, XPS, and PXRD further confirm that the chemical composition and crystalline structures remain intact after photocatalysis (Fig. S13–S17). In addition,

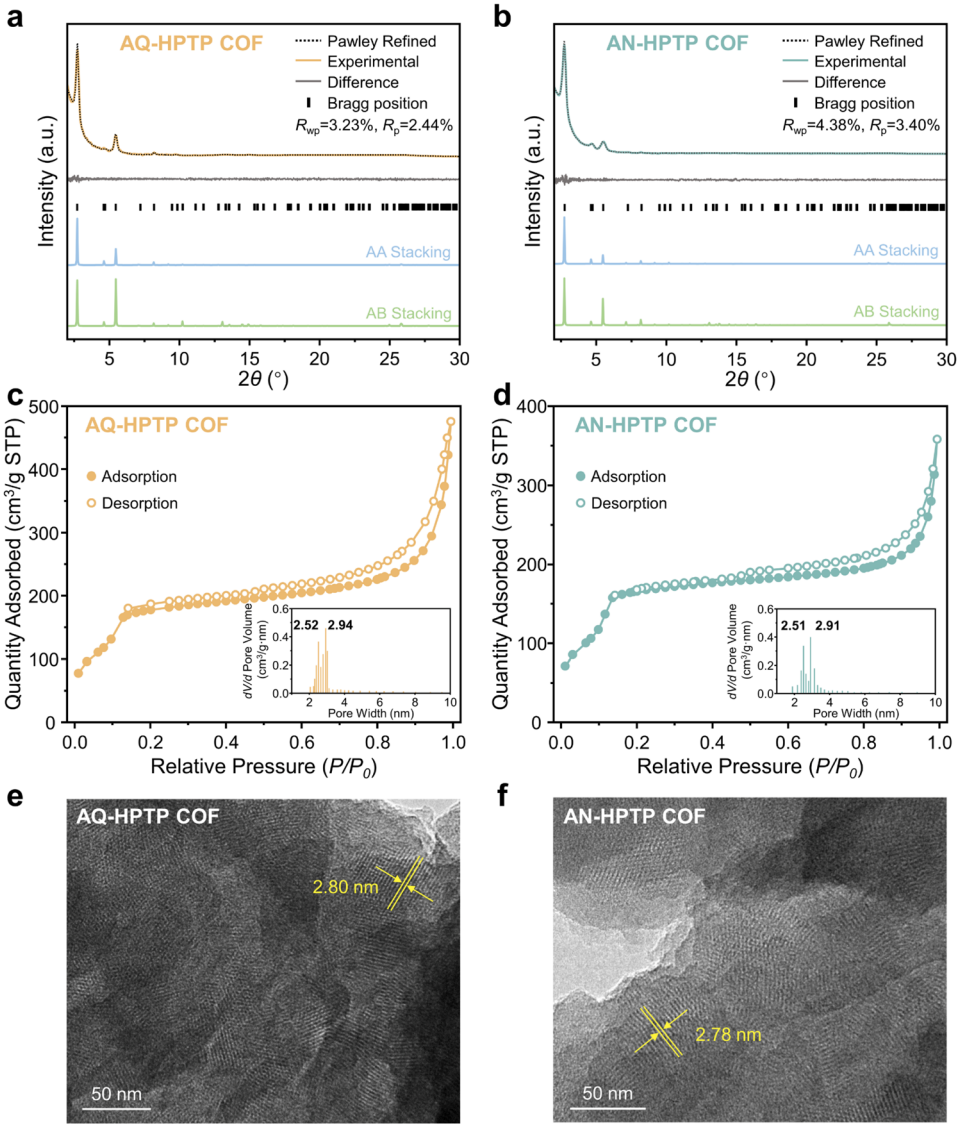

Fig. 2 Experimental and simulated PXRD patterns of (a) AQ-HPTP COF and (b) AN-HPTP COF. Pawley refined profiles and corresponding refinement differences are included for comparison. N_2 adsorption/desorption isotherms of (c) AQ-HPTP COF and (d) AN-HPTP COF. High-resolution TEM images of (e) AQ-HPTP COF and (f) AN-HPTP COF.

H_2O_2 retains over 95% of its concentration after 8 h of continuous illumination, indicating negligible catalyst-induced H_2O_2 decomposition under these conditions (Fig. S18).

Moreover, AQ-HPTP COF maintains efficient H_2O_2 production in municipal tap water and seawater collected from the East China Sea, indicating its strong potential for practical applications using realistic feedstocks (Fig. S19). Apparent quantum efficiencies (AQEs) measured under monochromatic irradiation decrease at longer wavelengths for both COFs, consistent with reduced absorption in this spectral region (Fig. S20).[34] Notably, AQ-HPTP COF reaches a peak AQE of 25.74% at 420 nm. Under AM 1.5G simulated sunlight, AQ-HPTP COF and AN-HPTP COF achieve SCC efficiencies of 2.10% and 0.79%, respectively. AQ-HPTP COF is among the very few COF photocatalysts that exceed 2% SCC for solar-driven H_2O_2 photosynthesis (Fig. 3d and Table S2). Importantly, the SCC efficiency of AQ-HPTP COF also surpasses previously reported AQ-containing photocatalysts (Table S3),[19,21] further demonstrating that integrating quinone redox centers into an hxl topology provides an effective route to maximize charge utilization and unlock the catalytic potential of AQ motifs in crystalline frameworks.

To assess practical applicability, we constructed a continuous-flow photocatalytic reactor for uninterrupted H_2O_2 production using AQ-HPTP COF (Fig. 3e and S21). The system comprises a quartz flow module integrating nine microreactors, coupled with a peristaltic pump and auxiliary components. Air-saturated water was continuously fed at 1 mL min^{-1}. Under visible light irradiation, the reactor operated steadily and produced an effluent H_2O_2 concentration of 2.4 mM for over 40 h (Fig. 3e). This sustained H_2O_2 concentration under continuous-flow operation is competitive with, and in many

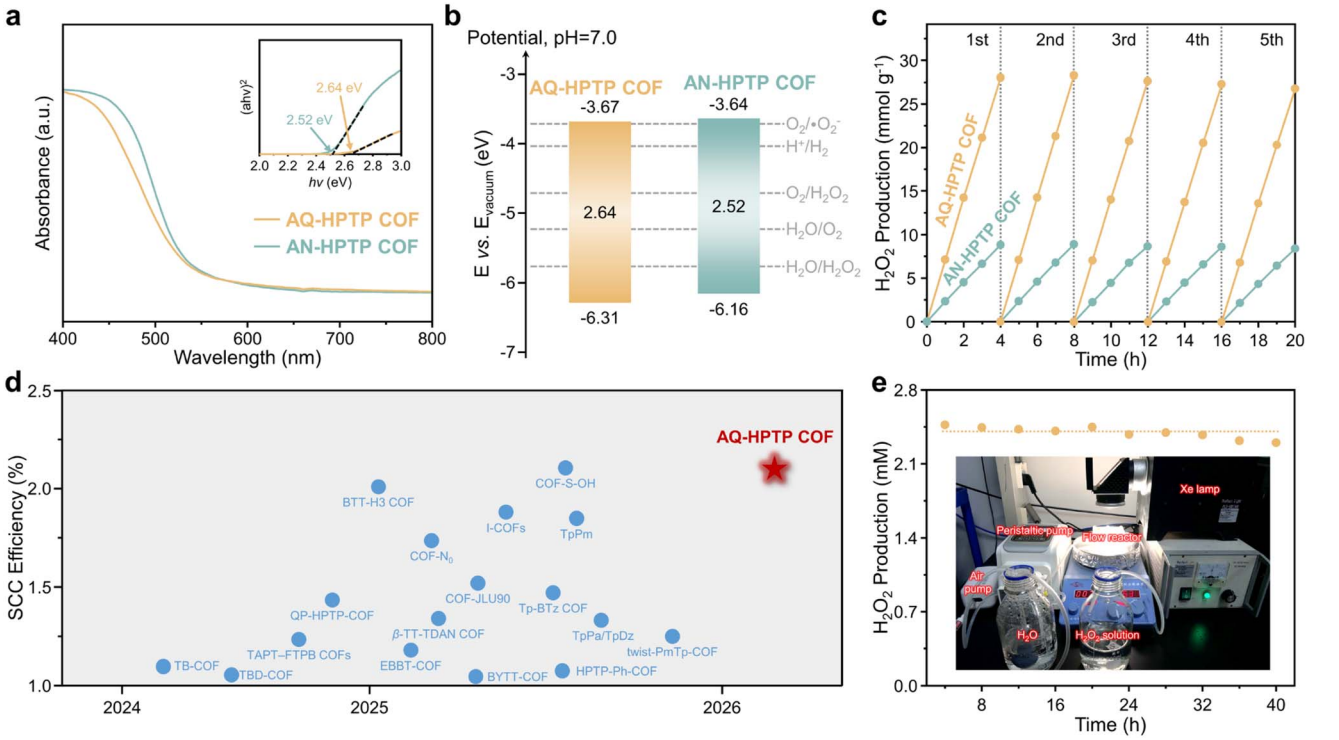

Fig. 3 (a) UV-vis-NIR diffuse reflectance spectra and (b) electronic band structures of both COFs. (c) Typical time course of overall photosynthetic H_2O_2 production for both COFs in O_2-saturated pure water under visible light irradiation ($\lambda > 420$ nm, 300 W Xe lamp). (d) Summarized COFs with SCC efficiencies exceeding 1% for solar-driven H_2O_2 production. (e) Typical time course of H_2O_2 production by AQ-HPTP COF in the continuous-flow photocatalytic reactor under visible light irradiation ($\lambda > 420$ nm, 300 W Xe lamp), the inset is the photograph of the continuous-flow photocatalytic reactor.

cases exceeds, those reported for COF-based photocatalytic systems (Table S4), reflecting the practical potential of AQ-HPTP COF. Post-reaction FTIR, solid-state NMR, XPS, PXRD and N_2 adsorption/desorption characterizations confirm that AQ-HPTP COF retains its chemical integrity and crystallinity after prolonged continuous operation (Fig. S22–S26). Thus, these results demonstrate that AQ-HPTP COF enables durable and continuous H_2O_2 production from ambient water and open-air oxygen under visible light irradiation.

The reaction pathways for photocatalytic H_2O_2 production over the two COFs were systematically examined. In O_2-saturated methanol solutions, both COFs produced H_2O_2 with yields that increased monotonically upon light irradiation, whereas no H_2 was detected in Ar-saturated solutions (Fig. S27), indicating that photogenerated electrons are preferentially consumed by ORR rather than proton reduction. Rotating disk electrode (RDE) measurements further reveal average electron-transfer numbers of 2.00 for AQ-HPTP COF and 2.03 for AN-HPTP COF during ORR (Fig. S28 and S29), consistent with a two-electron reduction pathway of O_2 to H_2O_2.[35] In line with this assignment, electron paramagnetic resonance (EPR) measurements using 5,5-dimethyl-1-pyrroline *N*-oxide (DMPO) as a spin trap show no detectable $\cdot O_2^-$ signal under illumination (Fig. S30), supporting a predominantly direct two-electron ORR mechanism rather than a stepwise one-electron route involving superoxide.[36]

On the water oxidation side, illumination of both COFs in Ar-saturated $NaIO_3$ aqueous solutions results exclusively in O_2 evolution (Fig. S31), consistent with a four-electron WOR pathway. This conclusion is further supported by complementary rotating ring-disk electrode (RRDE) and EPR analyses (Fig. S32 and S33).[37] Importantly, oxygen isotope labeling experiments demonstrate that the O_2 generated from WOR can be subsequently consumed in ORR to form H_2O_2 (Fig. S34), establishing a coupled redox cycle.[7] To further elucidate whether radical intermediates contribute to H_2O_2 formation, we performed scavenger control experiments using *p*-benzoquinone (BQ) as a $\cdot O_2^-$ quencher and *t*-butyl alcohol (TBA) as a $\cdot$OH scavenger.[38] As shown in Fig. S35, addition of either BQ or TBA produces no measurable change in the H_2O_2 production rates for either COF, indicating that neither $\cdot O_2^-$ nor $\cdot$OH plays a dominant role in the reaction pathway under our conditions.[39] These results indicate that both COFs achieve overall H_2O_2 photosynthesis by coupling direct two-electron ORR with four-electron WOR.

To elucidate the origin of the superior H_2O_2 photosynthesis performance of AQ-HPTP COF, we first examined how incorporation of the AQ moiety alters the frontier electronic structure. DFT calculations show that, in AQ-HPTP COF, the LUMO is predominantly localized on the AQ unit, whereas the HOMO is mainly distributed over the aromatic framework (Fig. 4a). This spatial separation is expected to promote photo-induced charge

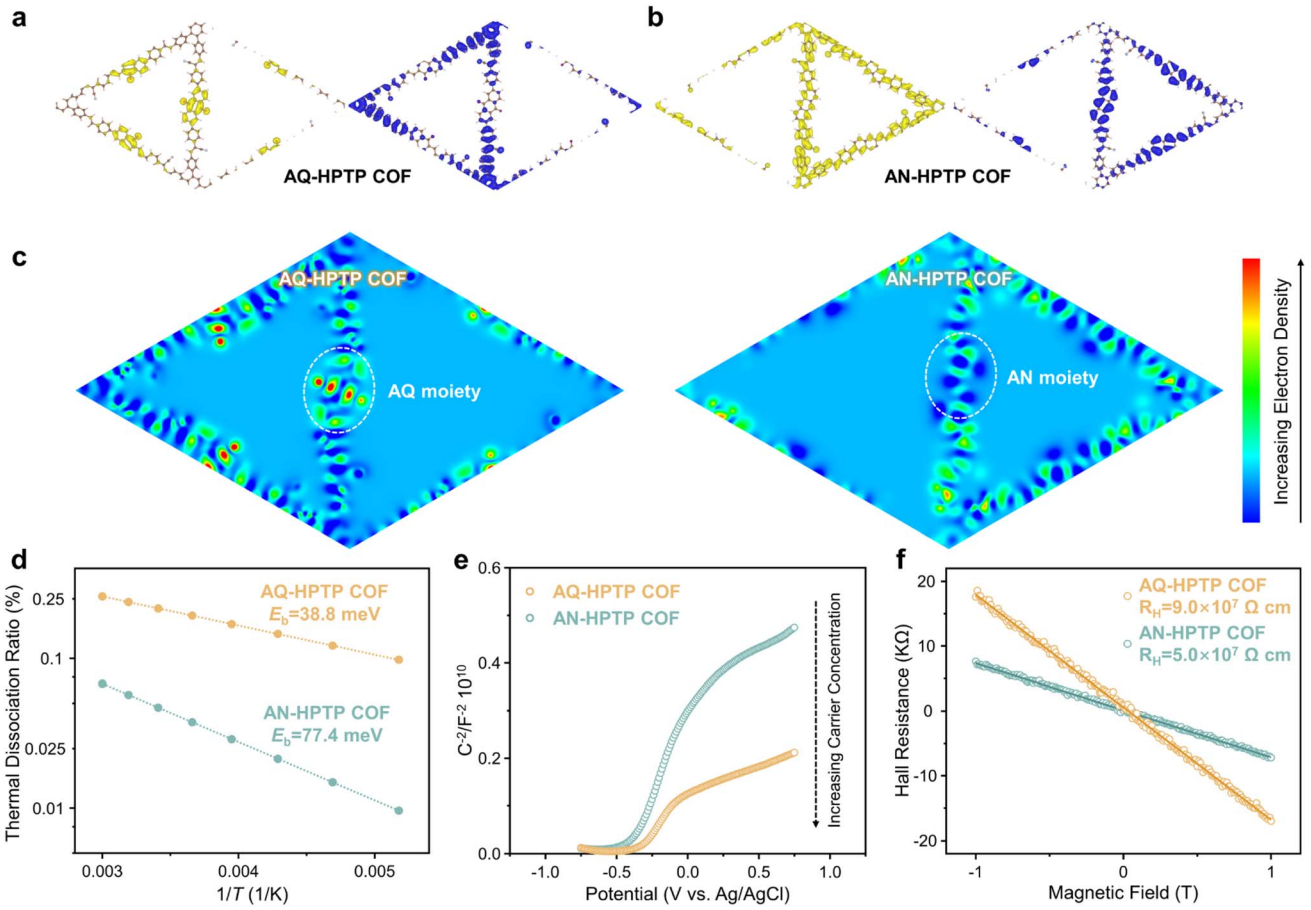

Fig. 4 Calculated LUMO and HOMO distributions of (a) AQ-HPTP COF and (b) AN-HPTP COF. Yellow and deep blue areas indicating electron and hole accumulation, respectively. (c) Calculated electron distributions in both COFs under photoexcitation. (d) Exciton dissociation rates in both COFs extracted from temperature-dependent PL spectra. (e) Mott–Schottky plots of both COFs under visible light irradiation (λ > 420 nm, 300 W Xe lamp). (f) Hall resistance *versus* magnetic field plots of both COFs at 298 K.

separation and directional intra-framework charge migration.[40] In contrast, AN-HPTP COF exhibits substantial overlap between HOMO and LUMO distributions (Fig. 4b), which is less favorable for charge separation. Meanwhile, excited-state electron density in AQ-HPTP COF is concentrated on the AQ moiety (Fig. 4c), whereas AN-HPTP COF does not display pronounced excited-state charge localization. These results suggest that the incorporation of AQ moiety substantially modified both the molecular orbitals arrangement and excited-state charge distribution that directs photogenerated electrons toward the AQ center.

We then quantified the impact of quinone incorporation on intrinsic charge-separation metrics. Temperature-dependent PL spectra reveals thermally activated PL quenching for both COFs (Fig. S36), enabling estimation of the E_b.[41] AQ-HPTP COF exhibits a substantially lower E_b (38.8 meV) than AN-HPTP COF (77.4 meV) (Fig. 4d and S37), indicating a reduced energetic barrier for exciton dissociation. Consistently, AQ-HPTP COF generates a higher transient photocurrent response than AN-HPTP COF under identical conditions (Fig. S38), consistent with more efficient separation and extraction of photogenerated charges.[42] Mott–Schottky analysis further indicates a higher apparent carrier density for AQ-HPTP COF, as reflected by the smaller slope at the same frequency (Fig. 4e).[43] EPR measurements using 2,2,6,6-tetramethyl-1-piperidinyloxy (TEMPO) as a redox-sensitive probe suggest a higher population of photogenerated electrons in AQ-HPTP COF under illumination (Fig. S39).[44] Solid-state EPR measurements also confirmed that AQ-HPTP COF generated more unpaired electrons than AN-HPTP COF (Fig. S40).[3] These results support that incorporation of AQ moiety markedly enhances charge separation and increases the availability of photogenerated electrons for interfacial O_2 reduction.

Charge transport is also a key parameter for sustained photocatalytic turnover in crystalline frameworks. Electrochemical impedance spectroscopy (EIS) shows a lower charge-transfer resistance for AQ-HPTP COF than for AN-HPTP COF (Fig. S41).[45] Open-circuit voltage decay (OCVD) measurements reveal a higher open-circuit photovoltage and slower decay for AQ-HPTP COF (Fig. S42), indicating extended carrier lifetimes, consistent with time-correlated single photon counting (TCSPC) results (Fig. S43).[46,47] Hall measurements confirm that both COFs behave as n-type semiconductors (negative Hall coefficients), with AQ-HPTP COF exhibiting a Hall mobility of 8.1 × 10^{-2} cm^2

V^{-1} s^{-1}, nearly twice that of AN-HPTP COF (4.3×10^{-2} cm^2 V^{-1} s^{-1}) (Fig. 4f). These results indicate that the AQ unit not only functions as a redox active site, but also improves charge separation/transport, thereby increasing overall charge utilization during H_2O_2 photosynthesis.

Given the pronounced differences in charge dynamics and photocatalytic activity, we next investigated the ORR active sites and reaction energetics in both COFs. DFT calculations were performed to compare O_2 adsorption energies across all plausible adsorption sites (Fig. S44, Tables S5 and S6). For AQ-HPTP COF, considering the quinone-specific proton-coupled electron transfer (PCET) chemistry, we also evaluated O_2 adsorption on AQH_2, the two-electron/proton accumulated state of AQ.[16,40,48] Notably, AQH_2 exhibits the most favorable O_2 adsorption among the examined sites, identifying the quinone unit as the most probable ORR center in AQ-HPTP COF. In contrast, for AN-HPTP COF, the cyano group in the cyanovinylene linkage is predicted to be the most favorable adsorption site for ORR. Importantly, the calculated O_2 adsorption energy on AQH_2 in AQ-HPTP COF (−0.397 eV) was substantially more negative than that on the cyano moiety in AN-HPTP COF (−0.056 eV), implying that AQ incorporation markedly enhances O_2 binding and can thereby facilitate O_2 activation under catalytic conditions.

We further analyzed the ORR free energy profiles (Fig. 5a). Both COFs are thermodynamically capable of direct two-electron ORR to H_2O_2. However, AQ-HPTP COF exhibits more favorable Gibbs free energy (ΔG) than AN-HPTP COF, consistent with its higher H_2O_2 production rate. *In situ* DRIFTS provides experimental validation of the predicted quinone redox intermediates. As shown in Fig. 5b, for AQ-HPTP COF, bands at 1670, 1487, and 1386 cm^{-1} are assigned to AQ, the one-electron accumulation state of AQ ($AQH\cdot$), and AQH_2, respectively.[16] Upon prolonged irradiation, the AQ peak gradually diminishes, whereas $AQH^{\bullet}$ and AQH_2 bands intensify progressively, indicating sequential photoinduced PCET at the AQ center. For AN-HPTP COF, the cyanovinylene C≡N band at 2214 cm^{-1} decreases under illumination (Fig. 5c), supporting participation of the cyano-linked moiety during H_2O_2 formation.[49] These results indicate that the two COFs operate through distinct ORR centers, with the AQ unit serving as the dominant reduction site in AQ-HPTP COF and the cyanovinylene linkage playing the corresponding role in AN-HPTP COF, while the framework topology remains essentially the same.

Because overall H_2O_2 photosynthesis requires hole consumption at the oxidation half-reaction, we next evaluated the four-electron WOR on both COFs. For the four-electron WOR, *OH formation from H_2O deprotonation is commonly the first uphill step, followed by formation of *O, *O*OH, and *OO* intermediates.[47] DFT screening indicates that in AQ-HPTP COF, feasible *OH formation is limited to a small number of sites, with the triphenylene unit emerging as the most probable WOR site among the candidates (Table S7 and Fig. S45). In AN-HPTP COF, the vinylene linkage is predicted to provide the most favorable energy for WOR (Table S8 and Fig. S45). After correcting free-energy profiles to reflect the practical oxidation potentials of photogenerated holes, the calculated WOR

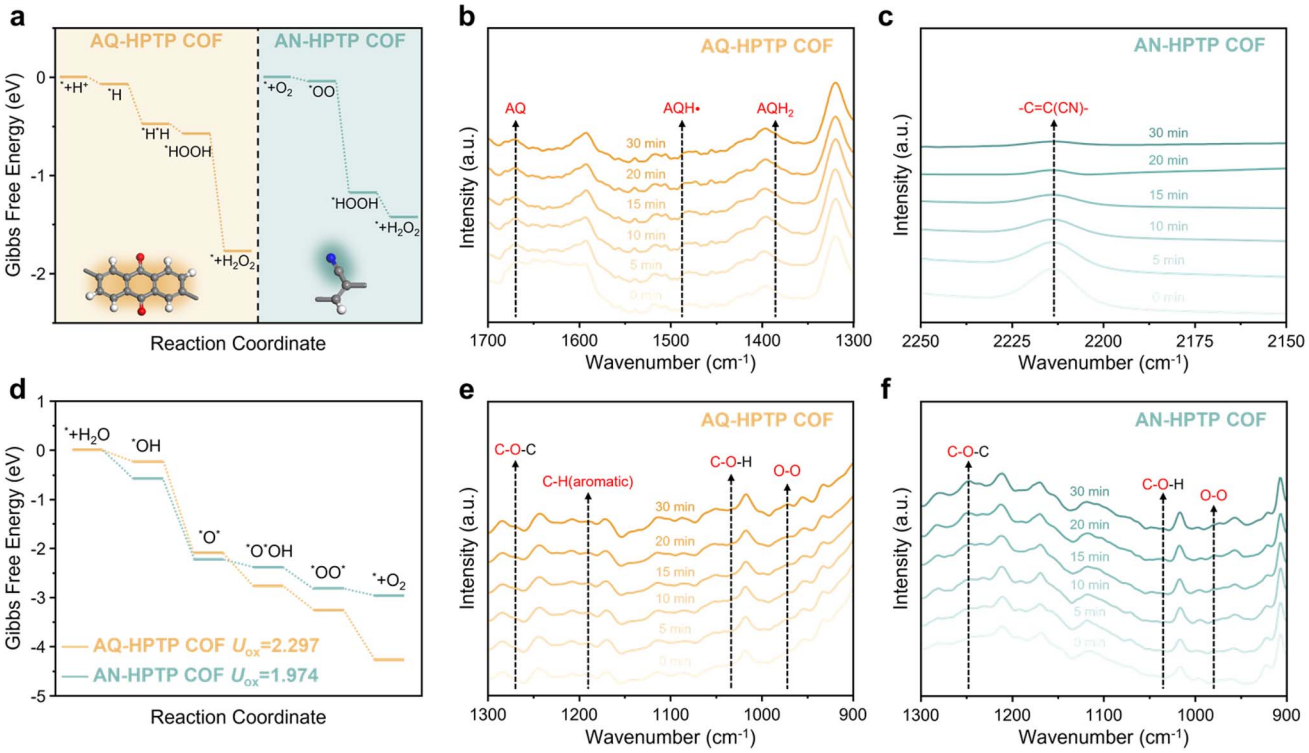

Fig. 5 (a) Calculated free energy diagrams of ORR pathways toward H_2O_2 production in both COFs. *In situ* DRIFT spectra of (b) AQ-HPTP COF and (c) AN-HPTP COF recorded during photocatalytic H_2O_2 production. (d) Calculated free energy diagrams of WOR pathway in both COFs. *In situ* DRIFT spectra recorded during photocatalytic H_2O_2 production on (e) AQ-HPTP COF and (f) AN-HPTP COF.

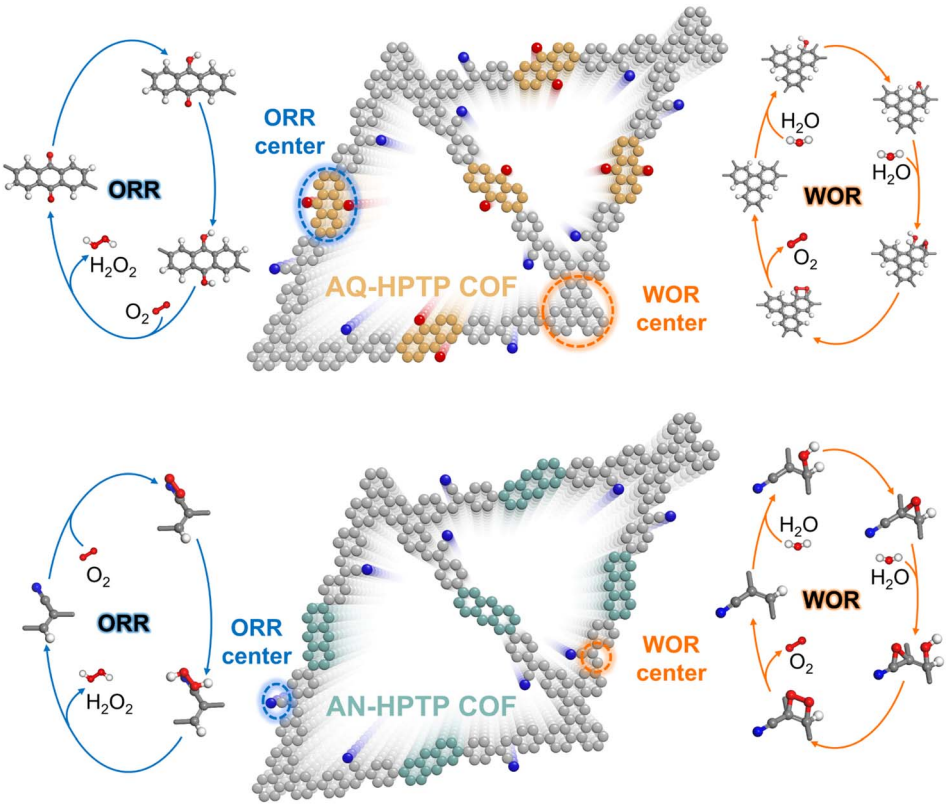

Scheme 1 Schematic illustration of photocatalytic reaction mechanisms toward H_2O_2 production on AQ-HPTP COF and AN-HPTP COF under visible light irradiation.

pathway on AQ-HPTP COF is thermodynamically more favorable than that on AN-HPTP COF (Fig. 5d), suggesting that AQ incorporation also modulates the oxidation energy landscape and can promote balanced redox turnover. Consistent with the theoretical predictions, *in situ* DRIFTS detects C–O stretching features attributable to C–O–H and C–O–C intermediate species after illumination (Fig. 5e and f), suggesting the occurrence of water oxidation to O_2.[24,50] In addition, peaks at 955–970 cm^{-1} associated with O–O vibrations further support that H_2O_2 formation proceeded predominantly through a direct two-electron ORR pathway on both COFs.[51]

Taken together, the combined spectroscopy and calculations reveal the mechanistic picture summarized in Scheme 1. In AQ-HPTP COF, the AQ moiety functions as the primary active center for direct two-electron ORR to H_2O_2 through sequential PCET, whereas the triphenylene moiety is the most probable WOR center. In AN-HPTP COF, the cyano group and the vinylene linkage are identified as the most likely ORR and WOR sites, respectively. Importantly, introducing AQ unit not only precisely defines the ORR active center but also enables spatial separation between reduction and oxidation sites, thereby leading to enhanced charge separation and transport. This architecture improves photogenerated charge utilization and underpins the markedly higher H_2O_2 photosynthesis efficiency of AQ-HPTP COF.

3 Conclusion

In conclusion, we designed and synthesized two fully π-conjugated COFs with hxl topology incorporating either an AQ unit or an AN analogue and employed them to photocatalytic H_2O_2 production. Incorporation of the AQ unit promotes intra-framework charge separation and steers excited-state electrons to the quinone-centered redox site, thereby enhancing charge utilization. In addition, proton-coupled reduction of the quinone substantially enhances O_2 binding, enabling more efficient oxygen activation and selective two-electron conversion to H_2O_2. Consequently, AQ-HPTP COF achieves an SCC efficiency of 2.10%, markedly exceeding those of previously reported COFs. Overall, these results demonstrate that the incorporation of quinone redox centers can enable concurrent optimization of charge dynamics and catalytic activity, providing a general molecular engineering strategy for advancing framework materials for solar-to-chemical energy conversion.

Conflicts of interest

The authors declare no conflicts of interest.

Author contributions

Wan Zhang: conceptualization, formal analysis, investigation, writing – original draft. Miao Sun: methodology, investigation,

software, writing – original draft. Lei Wang: funding acquisition, supervision, writing – review & editing. Xiaojun Wu: methodology, supervision, writing – review & editing. Hangxun Xu: funding acquisition, supervision, resources, project administration, writing – review & editing. All authors discussed the results and contributed to the final manuscript.

Data availability

The data supporting this article have been included as part of the supplementary information (SI). And data are available upon request from the authors. Supplementary information is available. See DOI: https://doi.org/10.1039/d6ta00399k.

Acknowledgements

This work was supported by the National Natural Science Foundation of China (52225307, U25A20265, and 22579158), the CAS Project for Young Scientists in Basic Research (YSBR-004), the open research fund of State Key Laboratory of Precision and Intelligent Chemistry, and the Fundamental Research Funds for the Central Universities (WK2060000099). We thank the Supercomputing Center of University of Science and Technology of China (USTC) for proving computational resources. This work was partially carried out at Instruments Center for Physical Science, University of Science and Technology of China.

References

1 X. Yu, Z. Wei, Y. Qin, X. Zhang, D. Hao, L. Jing, Y. Liu, H. Dai, J. Deng and Y. Zhu, *Adv. Mater.*, 2025, **37**, 2501494.
2 Z. Xie, X. Chen, W. Wang, X. Ke, X. Zhang, S. Wang, X. Wu, J. Yu and X. Wang, *Angew. Chem., Int. Ed.*, 2024, **63**, e202410179.
3 Y. Liu, L. Li, Z. Sang, H. Tan, N. Ye, C. Sun, Z. Sun, M. Luo and S. Guo, *Nat. Synth.*, 2025, **4**, 134–141.
4 R. Gao, M. Xia, Y. Deng, B. Yang, N. Huang, Y. Huang, H. Li, L. Bao, W. Liu, T. Ma and L. Ye, *Energy Environ. Sci.*, 2026, **19**, 539–550.
5 Y. Hou, F. Liu, J. Liang, Z. Li, P. Zhou and M. Tong, *Angew. Chem., Int. Ed.*, 2025, **64**, e202505621.
6 J. Yang, X. Zeng, M. Tebyetekerwa, Z. Wang, C. Bie, X. Sun, I. Marriam and X. Zhang, *Adv. Energy Mater.*, 2024, **14**, 2400740.
7 L. Zhang, C. Wang, Q. Jiang, P. Lyu and Y. Xu, *J. Am. Chem. Soc.*, 2024, **146**, 29943–29954.
8 Y. Cheng, H. Du, Y. Wang, J. Xin, Y. Dong, X. Wang, X. Zhou, B. Gui, J. Sun and C. Wang, *J. Am. Chem. Soc.*, 2025, **147**, 6355–6360.
9 X. Yan, F. Wang, X. Su, J. Ren, M. Qi, P. Bao, W. Chen, C. Peng and L. Chen, *Adv. Mater.*, 2023, **35**, 2305037.
10 R. Liu, Y. Chen, H. Yu, M. Položij, Y. Guo, T. C. Sum, T. Heine and D. Jiang, *Nat. Catal.*, 2024, **7**, 195–206.
11 J. Liao, M. Zhang, P. Huang, L. Dong, T. Ma, G. Huang, Y. Liu, M. Lu, S. Li and Y. Lan, *ACS Catal.*, 2024, **14**, 3778–3787.
12 E. Zhou, F. Wang, X. Zhang, Y. Hui and Y. Wang, *Angew. Chem., Int. Ed.*, 2024, **63**, e202400999.
13 J. Yue, Z. Xu, J. Luo, P. Yang and B. Tang, *ACS Catal.*, 2025, **15**, 12541–12550.
14 X. Ma, H. Pan, L. Gong, X. Ding, X. Zhou, H. Liu, R. Wang, C. Qu, Y. Zhao, D. Qi, Y. Bian and J. Jiang, *Angew. Chem., Int. Ed.*, 2025, **64**, e202511024.
15 R. Sun, X. Yang, X. Hu, Y. Guo, Y. Zhang, C. Shu, X. Yang, H. Gao, X. Wang, I. Hussain and B. Tan, *Angew. Chem., Int. Ed.*, 2024, **63**, e202416350.
16 Y. Huang, M. Shen, H. Yan, Y. He, J. Xu, F. Zhu, X. Yang, Y. Ye and G. Ouyang, *Nat. Commun.*, 2024, **15**, 5406.
17 H. Wang, L. Cao, X. Tao and G. Zhu, *Angew. Chem., Int. Ed.*, 2025, **64**, e202502943.
18 D. Wang, F. Tan, W. Zhao, S. Zhou, Q. Xu, L. Kan, L. Zhu, P. Gu and J. Lu, *Angew. Chem., Int. Ed.*, 2025, **64**, e202425017.
19 Y. Luo, C. Liu, J. Liu, X. Liu, Y. Zhou, X. Ou, B. Weng, J. Jiang and B. Han, *Chem. Eng. J.*, 2024, **481**, 148494.
20 X. Zhang, J. Zhang, J. Miao, X. Wen, C. Chen, B. Zhou and Y. Ling, *Chem. Eng. J.*, 2024, **466**, 143085.
21 X. Zhang, S. Cheng, C. Chen, X. Wen, J. Miao, B. Zhou, M. Long and L. Zhang, *Nat. Commun.*, 2024, **15**, 2649.
22 Z. Zhang, S. Bi, F. Meng, X. Li, M. Li, K. Mou, D. Wu and F. Zhang, *J. Am. Chem. Soc.*, 2023, **145**, 16704–16710.
23 S. Thomas, H. Li, C. Zhong, M. Matsumoto, W. R. Dichtel and J. Bredas, *Chem. Mater.*, 2019, **31**, 3051–3065.
24 J. Cheng, Y. Wu, W. Zhang, L. Wang, X. Wu and H. Xu, *Adv. Mater.*, 2025, **37**, 2410247.
25 S. Ma, Z. Li, Y. Hou, J. Li, Z. Zhang, T. Deng, G. Wu, R. Wang, S. Yang and X. Liu, *Angew. Chem., Int. Ed.*, 2025, **64**, e202501869.
26 Y. Xu, Y. Liu, X. Wang, H. Yang, P. Wang, W. Zhang, J. W. Ward and A. I. Cooper, *J. Mater. Chem. A*, 2025, **13**, 27524–27530.
27 S. Li, L. Li, Y. Li, L. Dai, C. Liu, Y. Liu, J. Li, J. Lv, P. Li and B. Wang, *ACS Catal.*, 2020, **10**, 8717–8726.
28 L. Zhang, Y. Huang, H. Yan, Y. Cheng, Y. Ye, F. Zhu and G. Ouyang, *Adv. Mater.*, 2024, **36**, 2401162.
29 Q. Zhang, K. Gu, C. Dong, C. Xue, H. Che, K. Zhang and Y. Ao, *Angew. Chem., Int. Ed.*, 2025, **64**, e202417591.
30 S. Ghosh, H. Küçükkeçeci, R. P. Paitandi, V. Weigelt, V. Dippold, S. Seki and A. Thomas, *J. Mater. Chem. A*, 2024, **12**, 247–255.
31 B. Gui, J. Xin, Y. Cheng, Y. Zhang, G. Lin, P. Chen, J. Ma, X. Zhou, J. Sun and C. Wang, *J. Am. Chem. Soc.*, 2023, **145**, 11276–11281.
32 H. Zheng, J. Ji, Y. Yusran, J. Chang, F. Chen, Z. Wang, J. Suo, J. Zhang, H. Li, D. Zhao, V. Valtchev, S. Qiu and Q. Fang, *J. Am. Chem. Soc.*, 2025, **147**, 13667–13676.
33 Z. Ding, J. Yang, Z. Wu, M. Adeli, X. Luo, X. Wang, X. Xie, X. Xu, C. Cheng and C. Zhao, *Chem. Mater.*, 2025, **37**, 1972–1982.
34 H. Wang, L. Song, M. Xu, F. Zhang, Z. Liu, G. Zheng and Q. Han, *Angew. Chem., Int. Ed.*, 2025, **64**, e202517545.
35 Q. Nan, J. Ning, B. Han, H. Wei, X. Wang, Y. Gu, S. Zhou, G. Cao, G. Zhang, X. Li, Y. Jia and L. Hao, *Chem. Sci.*, 2026, **17**, 466–474.

36 J. Zhang, F. Xue and Z. Wang, *Angew. Chem., Int. Ed.*, 2025, **64**, e202425617.
37 Z. Chen, H. Weng, C. Chu, D. Yao, Q. Li, C. Zhang and S. Mao, *Nat. Commun.*, 2025, **16**, 6943.
38 W. Ren, D. Chen, M. Zhang, X. Zhang and Z. Lan, *J. Mater. Chem. A*, 2025, **13**, 40239–40244.
39 C. Ru, J. Liang, Z. Lan, Z. Pan, W. Xing, S. Wang, Y. Hou and X. Wang, *Adv. Funct. Mater.*, 2026, **36**, e21894.
40 L. Wang, Y. Wu, S. Mao, J. Zhou, Y. Zhang, X. Zheng, X. Wu and H. Xu, *Adv. Mater.*, 2025, **37**, e08326.
41 Q. Zuo, B. Chu, X. Ye, F. Li, L. Li and Q. Xu, *J. Am. Chem. Soc.*, 2025, **147**, 34681–34689.
42 Z. Lin, X. Yu, Z. Zhao, N. Ding, C. Wang, K. Hu, Y. Zhu and J. Guo, *Nat. Commun.*, 2025, **16**, 1940.
43 R. Shen, X. Li, C. Qin, P. Zhang and X. Li, *Adv. Energy Mater.*, 2023, **13**, 2203695.
44 F. Liu, P. Zhou, Y. Hou, H. Tan, Y. Liang, J. Liang, Q. Zhang, S. Guo, M. Tong and J. Ni, *Nat. Commun.*, 2023, **14**, 4344.
45 X. Huang, W. Xie, T. Xu, W. Weng, T. Zhou and J. Guo, *Angew. Chem., Int. Ed.*, 2025, **64**, e202509095.
46 S. Li, R. Ma, S. Xu, T. Zheng, G. Fu, Y. Wu, Z. Liao, Y. Kuang, Y. Hou, D. Wang, P. Petkov, K. Simeonova, X. Feng, L. Wu, X. Li and T. Zhang, *J. Am. Chem. Soc.*, 2022, **144**, 13953–13960.
47 W. Zhang, M. Sun, J. Cheng, X. Wu and H. Xu, *Adv. Mater.*, 2025, **37**, 2500913.
48 P. Huang, Y. Peng, X. Wang, R. Li, M. Qin, M. Zhang, S. Wang, M. Lu, S. Li and Y. Lan, *Adv. Mater.*, 2026, **38**, e07849.
49 C. Qin, X. Wu, L. Tang, X. Chen, M. Li, Y. Mou, B. Su, S. Wang, C. Feng, J. Liu, X. Yuan and Y. Zhao, *Nat. Commun.*, 2023, **14**, 5238.
50 K. Xie, G. Wang, F. Huang, F. Zhao, J. Kan, Z. Chen, L. Cai, S. Han, Y. Geng and Y. Dong, *Nat. Commun.*, 2025, **16**, 3493.
51 W. Wu, Z. Li, S. Liu, D. Zhang, B. Cai, Y. Liang, M. Wu, Y. Liao and X. Zhao, *Angew. Chem., Int. Ed.*, 2024, **63**, e202404563.

